nanomaterials

MDPI

Article

Electrochemical Properties of an $Na_4Mn_9O_{18}$-Reduced Graphene Oxide Composite Synthesized via Spray Drying for an Aqueous Sodium-Ion Battery

Fuxing Yin [1], Zhengjun Liu [1], Yan Zhao [1,*], Yuting Feng [2] and Yongguang Zhang [1,*]

[1] School of Materials Science & Engineering, Research Institute for Energy Equipment Materials, Tianjin Key Laboratory of Materials Laminating Fabrication and Interface Control Technology, Hebei University of Technology, Tianjin 300130, China; yinfuxing@hebut.edu.cn (F.Y.); lzj125@126.com (Z.L.)

[2] Synergy Innovation Institute of GDUT, Heyuan 517000, China; 18222385469@163.com

* Correspondence: yanzhao1984@hebut.edu.cn (Y.Z.); yongguangzhang@hebut.edu.cn (Y.Z.); Tel.: +86-22-6020-1447; Fax: +86-22-6020-4064

Received: 17 August 2017; Accepted: 28 August 2017; Published: 2 September 2017

Abstract: An aqueous sodium ion battery (ASIB) with metal Zn as anode and $Na_4Mn_9O_{18}$-reduced graphene oxide ($Na_4Mn_9O_{18}$-RGO) as cathode has been developed. In this work, spherical $Na_4Mn_9O_{18}$-RGO composite particles were prepared via spray drying. The aqueous battery exhibits stable cyclability and high specific capacities. Typically, a high initial discharge capacity of 61.7 $mAh \cdot g^{-1}$ is attained at a high current rate of 4 C, and a stabilizing reversible capacity of 58.9 $mAh \cdot g^{-1}$ was obtained after 150 cycles. The network interlaced by RGO sheets provided fast electron conduction paths and structural stability to accommodate the mechanical stresses induced by sodium insertion and extraction, so the $Na_4Mn_9O_{18}$-RGO electrode displayed superior electrochemical performance in the ASIB.

Keywords: aqueous sodium-ion battery; cathode; $Na_4Mn_9O_{18}$; energy storage materials

1. Introduction

Recently, sodium-ion batteries (SIBs) have been regarded as promising candidates to lithium ion batteries (LIBs) due to the low cost, relative abundance of sodium [1,2], and analogous intercalation chemistry between sodium and lithium. However, some intrinsic drawbacks still exist in SIBs such as the slower diffusion efficiency in the Na-host materials due to the larger atomic mass of sodium, huge volume expansion, and serious pulverization of electrodes [3–5].

Thence, in order to meet the demand of good electrochemical performance, lots of SIB electrode materials have been developed. Various Na-Mn oxides such as $NaMn_{1/3}Ni_{1/3}Co_{1/3}PO_4$ [6], $Na_xMn_5O_{10}$ [7], $Na_2Mn_5O_{10}$ [8], and $Na_4Mn_9O_{18}$ have been extensively researched as active materials in SIB systems due to the presence of the extensive channels for Na ion intercalation and deintercalation [9]. Among them, $Na_4Mn_9O_{18}$ exhibits the MnO_6 octahedra and MnO_5 square cone, which are able to constitute the wide S-type double tunnels for Na ion diffusion [10]. Whitacre et al. reported the $Na_4Mn_9O_{18}$ as a positive electrode material for an aqueous sodium ion battery (ASIB), and this material cathode displayed a capacity of 45 $mAh \cdot g^{-1}$ at a current density of C/8 rate [11]. However, $Na_4Mn_9O_{18}$ displayed poor storage capability and cyclability owing to the large volume expansion during the intercalation/deintercalation of large Na^+, resulting in a gradual deterioration of dynamics and structures [12]. Encapsulating $Na_4Mn_9O_{18}$ into an elastic carbon matrix offers an ideal strategy to provide an electron pathway for individual particles while limiting surface reactions and reducing the stress associated with the volume change upon Na^+-ion insertion/extraction [13]. In 2012, hybrid aqueous lithium ion batteries with excellent cyclability and rate capability based on

a Zn metal anode and an $LiMn_2O_4$ cathode was reported by P. Chen's group [14]. Zn metal was chosen as an anode because of its abundance, low cost, and low equilibrium potential [15]. While referring to the literature corresponding to the similar system using a metallic Zn anode, the reversibility of the battery is reported to be a bit of a challenge in the presence of additives [16,17]. The environment of electrolyte has a great effect on the cyclic performance of zinc. Moreover, the acidic electrolyte is obviously different from the alkaline or neutral electrolytes [14].

The spray drying method possesses multitudinous strong points for controlling particle size and morphology, leading to a shortening of the evaporation time of the precursor and homogeneous composition [18]. Spray drying has been applied in the synthesis of numerous LIB cathodes, but it is rarely studied in SIB cathodes [19]. Herein, for the first time, we synthesized a novel $Na_4Mn_9O_{18}$-reduced graphene oxide ($Na_4Mn_9O_{18}$-RGO) composite with regular morphology and homogeneous composition via spray drying. Furthermore, we have investigated its potential as a positive electrode in an ASIB combining a Zn metal anode and an optimized Na^+/Zn^{2+} mixed-ion electrolytes.

2. Materials and Methods

2.1. The Preparation of $Na_4Mn_9O_{18}$-RGO Precursors by the HSCR Method

The $Na_4Mn_9O_{18}$-RGO composite precursors were prepared by a hydrothermal soft chemical reaction (HSCR) method with high NaOH concentration [20]. Firstly, 16.65 mL of a 2 mg/mL aqueous colloidal suspension of graphene oxide (GO) prepared by the Hummer's method [21] was added to 25 mL of a 0.28 M $MnSO_4$ aqueous solution while stirring. An equal volume of aqueous solution containing 3.0 M NaOH and 0.1 M $KMnO_4$ was then added into the above solution, and dark brown precipitates were quickly produced. The precipitate was washed once by deionized water and aged for 24 h to obtain Na-birnessite-GO precursors. Secondly, 4.0 g wet Na-birnessite-GO samples were added to 100 mL of a 15 M NaOH solution during a 30 min magnetic stirring period, and a dark brown suspension was then formed. Finally, the suspension was heated at 180 °C for 18 h using a 150 mL stainless steel autoclave with a Teflon liner. The resulting product was washed repeatedly with de-ionized water and dried at 60 °C in the air.

2.2. The Preparation of $Na_4Mn_9O_{18}$-RGO by Spray Drying

The spray drying system consists of atomizer, quartz reactor, and particle collector [22]. The prepared slurry was spray-dried by a spray drier system (HOLVES). The solution was transferred to a pneumatic atomizing nozzle by a peristaltic pump at 6 mL/min to form droplets. The moisture of the droplets was quickly evaporated after atomization in hot air. The entrance and exit temperatures of a spray drying machine were 200 and 110 °C, respectively. The feed solution was prepared with 0.6 g of prepared $Na_4Mn_9O_{18}$-RGO precursors in 200 mL of deionized water and mixed under mild ultra-sonication for 20 min to form a brown suspension. Then, the above suspension was spray-dried with an atomizing pressure of 0.8 MPa to produce the spray-dried powder.

Finally, the sample was further calcined under an Ar atmosphere for 2 h at 350 °C to form $Na_4Mn_9O_{18}$-RGO composite particles, as shown in the schematic diagram in Figure 1. Reference $Na_4Mn_9O_{18}$ particles without RGO was prepared following the same conditions.

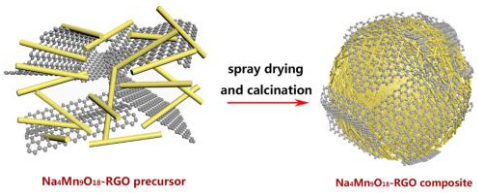

Figure 1. The schematic diagram of $Na_4Mn_9O_{18}$-RGO composite by spray drying.

2.3. Materials Characterization

The crystalline structure of as-prepared samples was characterized by X-ray diffraction (XRD, D8 Discover, Bruker, Germany) employing Cu Kα radiation. Raman spectra were attained with an Ar-ion laser of 532 nm using the inVia Reflex Raman imaging microscope system. Thermogravimetric analysis (TG, SDT Q-600, TA Instruments-Waters LLC, DE19720, Newcastle, PA, USA) was carried out from 25 to 1000 °C with a heating rate of 10 °C·min^{-1} under air. Scanning electron microscopy (SEM) analysis conducted on a Hitachi Limited S-4800 scanning electron microscope (Tokyo, Japan). The interior structure and selected area electron diffraction (SAED) of samples were studied using a JEOL JEM-2800 high resolution transmission electron microscope (HRTEM, Tokyo, Japan) at 160 kV.

2.4. Electrochemical Measurements

For preparing cathodes, the $Na_4Mn_9O_{18}$-RGO particles were blended with carbon black and polyvinylidene fluoride (PVDF) in a weight ratio of 8:1:1 in *N*-methyl-2-pyrrolidone (NMP). The above slurry was spread onto a graphite foil current collector and dried at 70 °C for 10 h. Disks with a diameter of 15 mm were cut with the active material of 3–3.5 mg. Zinc disks with a diameter of 15 mm were used as anodes. The electrolyte was a solution of 1 M Na_2SO_4 and 0.5 M $ZnSO_4$ with a pH level of 4 [23]. An absorbed glass mat (NSG Corporation, Tokyo, Japan) was used as a separator [24]. CR2025 cells were assembled in an air atmosphere before electrochemical tests were conducted. A battery tester (Neware, Shenzhen, China) was applied to investigate the charge/discharge cycling performances at different current densities in the voltage range of 1–1.85 V vs. Zn/Zn^{2+}. The electrochemical workstation (Princeton, VersaSTAT 4, 50/60 Hz, Ametek, PA, USA) was used to test the cyclic voltammogram (CV) in the voltage range of 1–2 V and the electrochemical impedance spectroscopy (EIS) in the frequency range of 0.01–100 kHz with an amplitude of 10 mV.

3. Result and Discussion

Figure 2 shows the XRD patterns of $Na_4Mn_9O_{18}$ and $Na_4Mn_9O_{18}$-RGO particles. The XRD pattern of the $Na_4Mn_9O_{18}$ sample are in good agreement with those of orthorhombic $Na_4Mn_9O_{18}$ in accordance with JCPDS #27-0750 [25]. The obtained lattice parameters are a = 9.1 Å, b = 26.34 Å, and c = 2.821 Å, which are consistent with previous reports [25,26]. For the $Na_4Mn_9O_{18}$-RGO sample, two broad diffraction peaks at around 25.8° and 43.1° can be seen, which are associated with the planes (200) and (100) of the RGO structure [27]. Apart from $Na_4Mn_9O_{18}$ and RGO, no foreign peaks from impurities were observed.

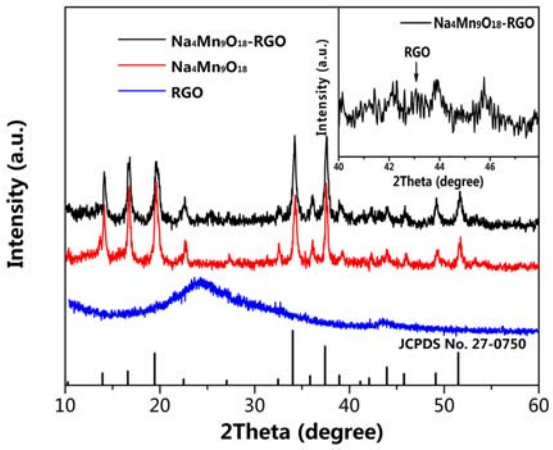

Figure 2. XRD patterns of $Na_4Mn_9O_{18}$, $Na_4Mn_9O_{18}$-RGO, and RGO.

$Na_4Mn_9O_{18}$ and $Na_4Mn_9O_{18}$-RGO particles were further determined by Raman spectra (Figure 3). The broad bands at around 615 cm^{-1} may be associated with stretching vibrations of Mn–O [13]. Compared to the spectrum of $Na_4Mn_9O_{18}$, $Na_4Mn_9O_{18}$-RGO contained two carbon-related bands at about 1352 (D-band) and 1594 cm^{-1} (G-band). These bands could be due to defective or disorder carbon and graphitic carbon in RGO, respectively [28,29].

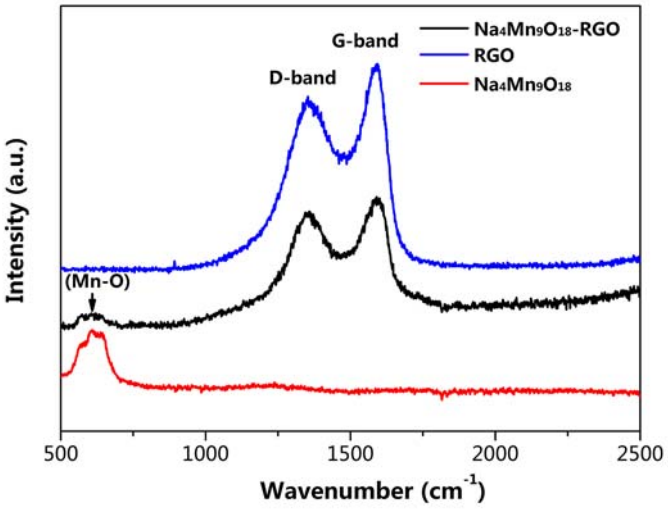

Figure 3. Raman spectrum of $Na_4Mn_9O_{18}$, $Na_4Mn_9O_{18}$-RGO, and RGO.

The TG and DTG data is collected and shown in Figure 4. The first mass loss about 7% from room temperature to 200 °C is related to the release of physically absorbed water. The second mass loss that appears from 200 to 750 °C is due to the oxidation of C to CO_2. As we can see, the TG curves of the $Na_4Mn_9O_{18}$-RGO, the weight fractions of $Na_4Mn_9O_{18}$ and RGO were recorded to be 81.7% and 18.3%, respectively.

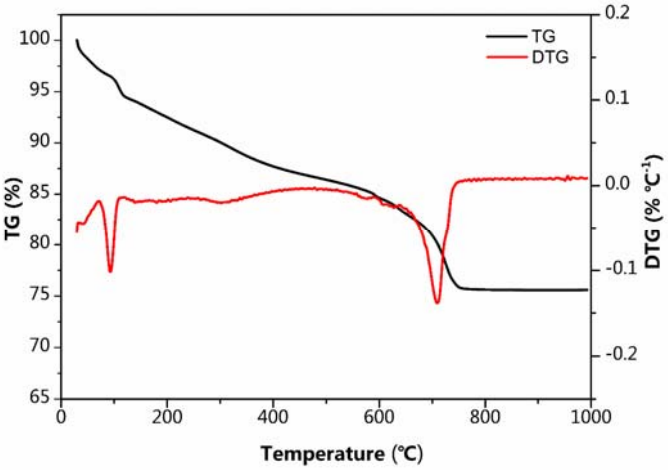

Figure 4. TG-DTG curves of $Na_4Mn_9O_{18}$-RGO under an air atmosphere.

Figure 5 shows the morphology and structure of $Na_4Mn_9O_{18}$-RGO, which was confirmed by SEM and TEM. As shown in Figure 5a, the $Na_4Mn_9O_{18}$-RGO samples present a spherical or ellipsoidal shape with diameters of about 4–6 μm. The inset image of Figure 5a indicates that the $Na_4Mn_9O_{18}$-RGO particle has a diameter of 4.66 μm, with rod-like $Na_4Mn_9O_{18}$ intimately wrapped in lamellarly structured RGO forming a spherical morphology. In addition, Figure 5b shows clearly the crosslinking state of $Na_4Mn_9O_{18}$ and RGO. The rod-shaped $Na_4Mn_9O_{18}$ with a diameter of around

50–80 nm are intertwined together by RGO, which will enhance the electrical conductivity of the micron-sized composite. The HRTEM image in Figure 5c shows the vertical lattice fringe is 0.45 nm, which corresponds to the (200) crystallographic plane of $Na_4Mn_9O_{18}$ [12]. The SAED pattern in Figure 5d indicates the single crystal nature of $Na_4Mn_9O_{18}$ and the polycrystalline of RGO, which is due to the multi-layer stacking.

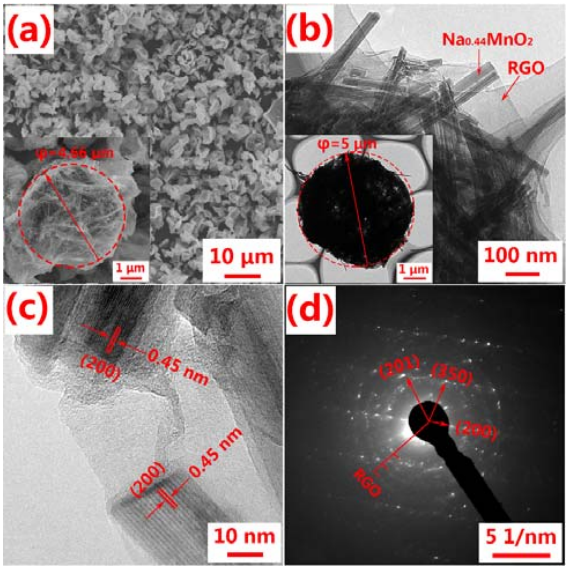

Figure 5. The morphology and structure of the $Na_4Mn_9O_{18}$-RGO. (**a**) SEM image; (**b**) TEM image; (**c**) HRTEM image; (**d**) SAED pattern.

Figure 6a shows the CV curves of $Na_4Mn_9O_{18}$-RGO at a rate of 0.1 $mV \cdot s^{-1}$. There are two reduction peaks at around 1.18–1.19 V and 1.35–1.37 V as well as one oxidation peak at about 1.55–1.6 V during the first four cycles. With increasing cycles, the potentials of the redox peak increase and tend to be stable. In addition, the reduction peak at about 1.18–1.19 V gradually disappeared while the peak at 1.35–1.37 V gradually increased due to the initial activation process of the electrode. The charge and discharge curves are displayed in Figure 6b. The $Na_4Mn_9O_{18}$-RGO electrode shows two potential plateaus at about 1.18 and 1.36 V in its discharge process and one plateau at around 1.55 V in its charging cycle, corresponding well with the CV data. The initial coulombic efficiency was only 77.6% due to the high initial charge capacity of 79.5 $mAh \cdot g^{-1}$, which originates from the irreversible side reactions that occurred in the first charge process. The first four discharge curves exhibited an excellent discharge capacity of around 63 $mAh \cdot g^{-1}$ at a high current density of 4 C.

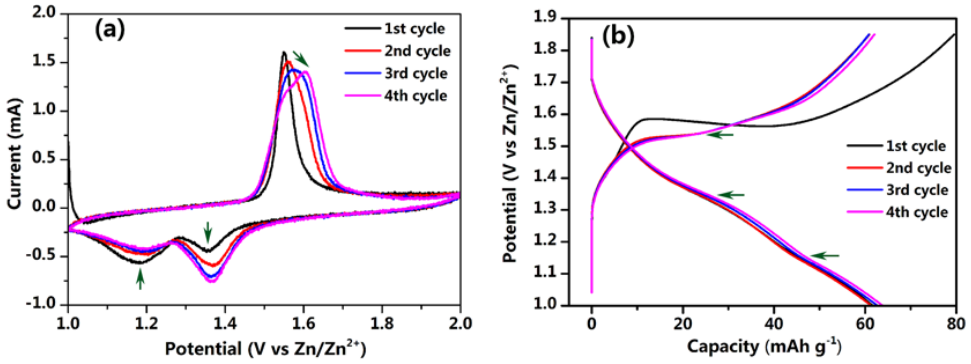

Figure 6. Electrochemical performance of the $Na_4Mn_9O_{18}$-RGO electrode (vs. Zn/Zn^{2+}). (**a**) CV curves at a rate of 0.1 $mV \cdot s^{-1}$. (**b**) Charge and discharge curves at 4 C.

Figure 7a presents the cycling performance of the $Na_4Mn_9O_{18}$-RGO and $Na_4Mn_9O_{18}$ electrodes at 4 C. Both type of electrodes experienced a drop in capacity from the first cycle, which corresponding to the electrodes activation process. The initial discharge capacity of the $Na_4Mn_9O_{18}$-RGO electrode was 61.7 mAh·g^{-1}, and the maximum capacity was 80.5 mAh·g^{-1} in the 35th cycle. The $Na_4Mn_9O_{18}$-RGO and $Na_4Mn_9O_{18}$ electrodes both exhibited good cycle stability, maintaining a specific capacity of 58.9 and 41.2 mAh g^{-1} after 150 cycles. Compared with the initial cycle, the two electrodes maintained a capacity of 95.5% and 83.2% after 150 cycles, respectively. For the $Na_4Mn_9O_{18}$-RGO electrode, the addition of RGO is necessary for mitigating the low electronic conductivity of $Na_4Mn_9O_{18}$ [30].

The rate capability of the $Na_4Mn_9O_{18}$-RGO and $Na_4Mn_9O_{18}$ electrodes are investigated and compared in Figure 7b. As expected, compared with the $Na_4Mn_9O_{18}$ electrode, the $Na_4Mn_9O_{18}$-RGO electrode represents a better rate performance. The $Na_4Mn_9O_{18}$-RGO electrode submits a reversible discharge capacity of around 85 mAh·g^{-1} at a 1 C low current rate. Furthermore, the $Na_4Mn_9O_{18}$-RGO electrode can deliver reversible discharge capacities of 75, 68, and 61 mAh g^{-1} at the rates of 2, 3, and 4 C, respectively. Surprisingly, when the current rate was returned to 1 C, the specific discharge capacity of the composite recovered to 94 mAh·g^{-1}. This is equivalent to a 110.6% recovery of the initial capacity, corresponding to the electrodes activation process in Figure 7a, suggesting good electrode structure stability of the $Na_4Mn_9O_{18}$-RGO electrode. As a comparison, the reversible discharge capacities of the $Na_4Mn_9O_{18}$ at each current rate were lower than that of the $Na_4Mn_9O_{18}$-RGO. It can be concluded that the network interlaced by RGO sheets provides fast electron conduction pathways and structural stability to accommodate the mechanical stresses induced by sodium insertion and extraction.

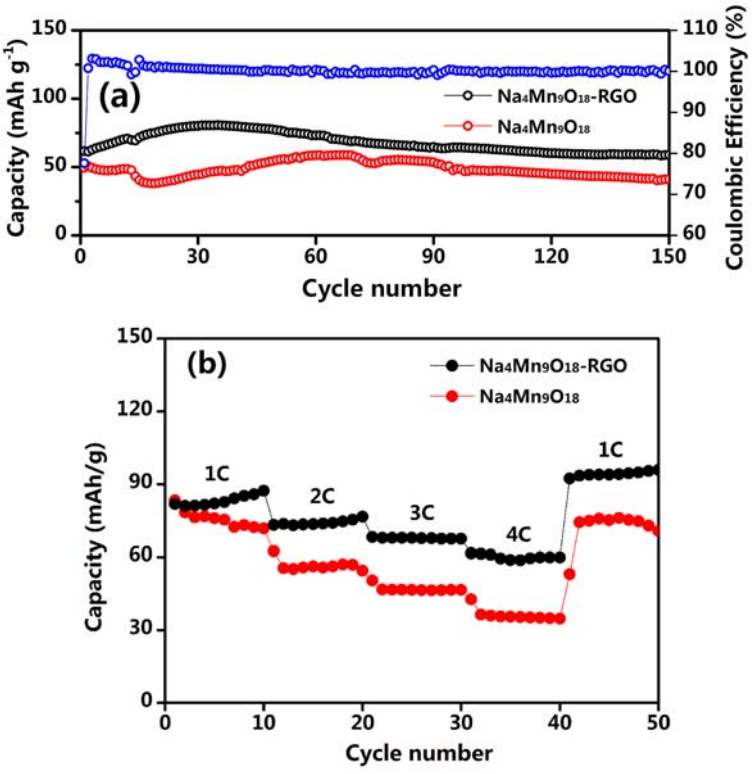

Figure 7. (**a**) Cycling performance of the $Na_4Mn_9O_{18}$-RGO and $Na_4Mn_9O_{18}$ electrodes at 4 C and coulombic efficiency of the $Na_4Mn_9O_{18}$-RGO electrode. (**b**) Rate capability of the $Na_4Mn_9O_{18}$-RGO and $Na_4Mn_9O_{18}$ electrodes.

Nyquist plots of the $Na_4Mn_9O_{18}$-RGO and $Na_4Mn_9O_{18}$ electrodes were produced with a frequency range of 10^5–0.01 Hz and are presented in Figure 8. The inset of Figure 8 is a simple equivalent circuit model applied to fit the EIS.

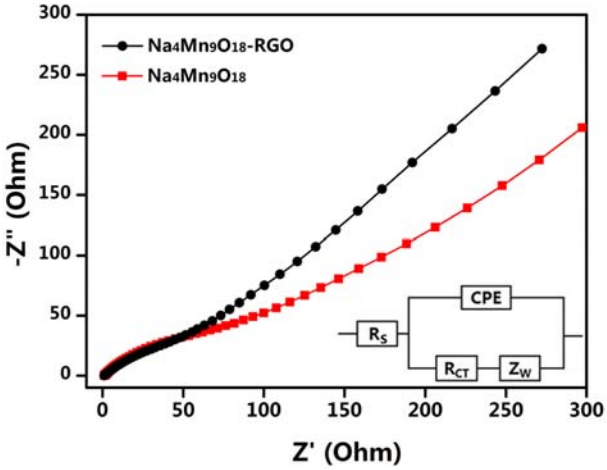

Figure 8. EIS of the $Na_4Mn_9O_{18}$-RGO and $Na_4Mn_9O_{18}$ electrodes and the equivalent circuit model of plot fitting (inset).

The R_S is the electrolyte resistance of cell components, R_{CT} is associated with the charge transfer procedure at the electrode-electrolyte interface, Z_W is the Warburg impedance that is associated with sodium-ion diffusion in the electrode, and CPE is associated with the double layer capacitance. It can be seen that the charge transfer resistance (R_{CT}) of the $Na_4Mn_9O_{18}$-RGO electrode is a little smaller than that of $Na_4Mn_9O_{18}$. Additionally, the Z_W of the $Na_4Mn_9O_{18}$-RGO electrode has a bigger slope, which indicates enhanced sodium-ion diffusion. Our EIS measurements demonstrated that the RGO sheets are beneficial to improving electrochemical performance.

4. Conclusions

In summary, the $Na_4Mn_9O_{18}$-RGO particles have been successfully synthesized by a hydrothermal soft chemical reaction and via spray drying. An aqueous sodium ion battery using metallic Zn and $Na_4Mn_9O_{18}$-RGO as the negative and positive electrodes, respectively, has been developed. Compared to the $Na_4Mn_9O_{18}$ electrode, the $Na_4Mn_9O_{18}$-RGO electrode offered a larger discharge capacity of 58.9 $mAh \cdot g^{-1}$ at 4 C, even after 150 full cycles due to the network structure of RGO. The superior electrochemical performance demonstrates that $Na_4Mn_9O_{18}$-RGO can be a promising material for a safe and efficient ASIB.

Acknowledgments: This work was supported by grants from the National Natural Science Foundation of China (Grant No. 21406052), the Science Research Foundation for Selected Overseas Chinese Scholars, the Ministry of Human Resources and Social Security of China (Grant No. CG2015003002), and the Program for the Outstanding Young Talents of Hebei Province (Grant No. BJ2014010).

Author Contributions: Fuxing Yin and Yongguang Zhang conceived and designed the experiments; Zhengjun Liu and Yuting Feng carried out the experiments; Zhengjun Liu and Yan Zhao analyzed the data; Fuxing Yin and Yongguang Zhang contributed reagents/materials/analysis tools; Yongguang Zhang and Yan Zhao contributed in the drafting and revision of the manuscript.

Conflicts of Interest: The authors declare no conflict of interest.

References

1. Zhang, B.; Liu, Y.; Wu, X.; Yang, Y.; Chang, Z.; Wen, Z.; Wu, Y. Cheminform abstract: An aqueous rechargeable battery based on zinc anode and $Na_{0.95}MnO_2$. *Chem. Commun.* **2014**, *45*, 1209–1211. [CrossRef] [PubMed]
2. Li, Z.; Young, D.; Xiang, K.; Carter, W.C.; Chiang, Y.M. Towards high power high energy aqueous sodium-ion batteries: The $NaTi_2(PO_4)_3/Na_{0.44}MnO_2$ System. *Adv. Energy Mater.* **2013**, *3*, 290–294. [CrossRef]
3. Li, S.; Dong, Y.; Xu, L.; Xu, X.; He, L.; Mai, L. Effect of carbon matrix dimensions on the electrochemical properties of $Na_3V_2(PO_4)_3$ nanograins for high-performance symmetric sodium-ion batteries. *Adv. Mater.* **2014**, *26*, 3545–3553. [CrossRef] [PubMed]

4. Hong, S.Y.; Kim, Y.; Park, Y.; Choi, A.; Choi, N.S.; Lee, K.T. ChemInform Abstract: Charge Carriers in Rechargeable Batteries: Na Ions vs. Li Ions. *Energy Environ. Sci.* **2014**, *45*, 2067–2081. [CrossRef]
5. Cao, Y.; Xiao, L.; Wang, W.; Choi, D.; Nie, Z.; Yu, J.; Saraf, L.V.; Yang, Z.; Liu, J. Reversible sodium ion insertion in single crystalline manganese oxide nanowires with long cycle life. *Adv. Mater.* **2011**, *23*, 3155–3160. [CrossRef] [PubMed]
6. Minakshi, M.; Meyrick, D.; Appadoo, D. Maricite ($NaMn_{1/3}Ni_{1/3}Co_{1/3}PO_4$)/activated carbon: Hybrid capacitor. *Energy Fuel* **2013**, *27*, 3516–3522. [CrossRef]
7. Minakshi, M. Looking beyond lithium-ion technology-aqueous NaOH battery. *Mater. Sci. Eng. B* **2012**, *177*, 1788–1792. [CrossRef]
8. Liu, S.; Fan, C.Z.; Zhang, Y.; Li, C.H.; You, X.Z. Low-temperature synthesis of $Na_2Mn_5O_{10}$ for supercapacitor applications. *J. Power Sources* **2011**, *196*, 10502–10506. [CrossRef]
9. Datta, M.K.; Kuruba, R.; Jampani, P.H.; Chung, S.J.; Saha, P.; Epur, R.; Kadakia, K.; Patel, P.; Gattu, B.; Manivannan, A. Electrochemical properties of a new nanocrystalline $NaMn_2O_4$ cathode for rechargeable sodium ion batteries. *Mater. Sci. Eng. B-Adv.* **2014**, *188*, 1–7. [CrossRef]
10. Saint, J.A.; Doeff, M.M.; Wilcox, J. Electrode materials with the $Na_{0.44}MnO_2$ structure: Effect of titanium substitution on physical and electrochemical properties. *Chem. Mater.* **2008**, *20*, 3404–3411. [CrossRef]
11. Whitacre, J.F.; Tevar, A.; Sharma, S. $Na_4Mn_9O_{18}$ as a positive electrode material for an aqueous electrolyte sodium-ion energy storage device. *Electrochem. Commun.* **2010**, *12*, 463–466. [CrossRef]
12. Fu, B.; Zhou, X.; Wang, Y. High-rate performance electrospun $Na_{0.44}MnO_2$ nanofibers as cathode material for sodium-ion batteries. *J. Power Sources* **2016**, *310*, 102–108. [CrossRef]
13. Zhao, L.; Ni, J.; Wang, H.; Gao, L. $Na_{0.44}MnO_2$-CNT electrodes for non-aqueous sodium batteries. *RSC. Adv.* **2013**, *3*, 6650–6655. [CrossRef]
14. Yan, J.; Wang, J.; Liu, H.; Bakenov, Z.; Gosselink, D.; Chen, P. Rechargeable hybrid aqueous batteries. *J. Power Sources* **2012**, *216*, 222–226. [CrossRef]
15. Lee, J.S.; Sun, T.K.; Cao, R.; Choi, N.S.; Liu, M.; Lee, K.T.; Cho, J. Metal-air batteries: Metal-air batteries with high energy density: Li-air versus Zn-air. *Adv. Energy Mater.* **2011**, *1*, 34–50. [CrossRef]
16. Minakshi, M.; Mitchell, D.R.G.; Prince, K. Incorporation of TiB_2 additive into MnO_2 cathode and its influence on rechargeability in an aqueous battery system. *Solid State Ion.* **2008**, *179*, 355–361. [CrossRef]
17. Minakshi, M.; Pandey, A.; Blackford, M.; Ionescu, M. Effect of TiS_2 additive on $LiMnPO_4$ cathode in aqueous solutions. *Energy Fuel* **2010**, *24*, 6193–6197. [CrossRef]
18. Zou, H.; Li, S.; Wu, X.; Mcdonald, M.J.; Yang, Y. Spray-drying synthesis of pure Na_2CoPO_4F as cathode material for sodium ion batteries. *ECS Electrochem. Lett.* **2015**, *4*, A53–A55. [CrossRef]
19. Wu, F.; Wang, Z.; Li, X.; Guo, H.; Peng, Y.; Xiong, X.; He, Z.; Zhang, Q. Characterization of spherical-shaped $Li_4Ti_5O_{12}$ prepared by spray drying. *Electrochim. Acta* **2012**, *78*, 331–339. [CrossRef]
20. Liu, C.; Guo, W.L.; Wang, Q.H.; Li, J.G.; Yang, X.P. Parametric study of hydrothermal soft chemical synthesis and application of $Na_{0.44}MnO_2$ nanorods for Li-ion battery cathode materials: Synthesis conditions and electrochemical performance. *J. Alloys Compd.* **2016**, *658*, 588–594. [CrossRef]
21. Guerrero-Contreras, J.; Caballero-Briones, F. Graphene oxide powders with different oxidation degree, prepared by synthesis variations of the Hummers method. *Mater. Chem. Phys.* **2015**, *153*, 209–220. [CrossRef]
22. Ju, S.H.; Yun, C.K. Effects of drying control chemical additive on properties of $Li_4Ti_5O_{12}$ negative powders prepared by spray pyrolysis. *J. Power Sources* **2010**, *195*, 4327–4331. [CrossRef]
23. Bai, S.; Song, J.; Wen, Y.; Cheng, J.; Cao, G.; Yang, Y.; Li, D. Effects of zinc and manganese ions in aqueous electrolytes on structure and electrochemical performance of $Na_{0.44}MnO_2$ cathode material. *RSC Adv.* **2016**, *6*, 40793–40798. [CrossRef]
24. Yesibolati, N.; Umirov, N.; Koishybay, A.; Omarova, M.; Kurmanbayeva, I.; Zhang, Y.; Zhao, Y.; Bakenov, Z. High performance Zn/$LiFePO_4$ aqueous rechargeable battery for large scale applications. *Electrochim. Acta* **2015**, *152*, 505–511. [CrossRef]
25. Dong, J.K.; Ponraj, R.; Kannan, A.G.; Lee, H.W.; Fathi, R.; Ruffo, R.; Mari, C.M.; Kim, D.K. Diffusion behavior of sodium ions in $Na_{0.44}MnO_2$ in aqueous and non-aqueous electrolytes. *J. Power Sources* **2013**, *244*, 758–763.
26. Liu, C.; Li, J.; Zhao, P.; Guo, W.; Yang, X. Fast preparation of $Na_{0.44}MnO_2$ nanorods via a high NaOH concentration hydrothermal soft chemical reaction and their lithium storage properties. *J. Nanopart. Res.* **2015**, *17*, 142. [CrossRef]

27. Veerappan, G.; SunyoungYoo; Zhang, K.; Ma, M.; Kang, B.; Park, J.H. High-reversible capacity of perovskite $BaSnO_3$/rGO composite for lithium-ion battery anodes. *Electrochim. Acta* **2016**, *214*, 31–37. [CrossRef]
28. Bharathidasan, P.; Kim, D.W.; Devaraj, S.; Sivakkumar, S.R. Supercapacitive characteristics of carbon-based graphene composites. *Electrochim. Acta* **2016**, *204*, 146–153. [CrossRef]
29. Dresselhaus, M.S.; Jorio, A.; Hofmann, M.; Dresselhaus, G.; Saito, R. Perspectives on carbon nanotubes and graphene raman spectroscopy. *Nano Lett.* **2010**, *10*, 751–758. [CrossRef] [PubMed]
30. Liu, Y.; He, D.; Wu, H.; Duan, J.; Zhang, Y. Hydrothermal self-assembly of manganese dioxide/manganese carbonate/reduced graphene oxide aerogel for asymmetric supercapacitors. *Electrochim. Acta* **2015**, *164*, 154–162. [CrossRef]